Earth and Planetary Science Letters 485 (2018) 111–120

Contents lists available at ScienceDirect

Earth and Planetary Science Letters

www.elsevier.com/locate/epsl

# Relationships between $CO_2$, thermodynamic limits on silicate weathering, and the strength of the silicate weathering feedback

Matthew J. Winnick*, Kate Maher

*Department of Geological Sciences, Stanford University, Stanford, CA, USA*

ARTICLE INFO

*Article history:*
Received 31 July 2017
Received in revised form 5 January 2018
Accepted 6 January 2018
Editor: D. Vance

*Keywords:*
chemical weathering
negative feedback
thermodynamic limits
carbon cycle
geobiology
paleoclimate

ABSTRACT

Recent studies have suggested that thermodynamic limitations on chemical weathering rates exert a first-order control on riverine solute fluxes and by extension, global chemical weathering rates. As such, these limitations may play a prominent role in the regulation of carbon dioxide levels ($pCO_2$) over geologic timescales by constraining the maximum global weathering flux. In this study, we develop a theoretical scaling relationship between equilibrium solute concentrations and $pCO_2$ based on equilibrium constants and reaction stoichiometry relating primary mineral dissolution and secondary mineral precipitation. We test this theoretical scaling relationship against reactive transport simulations of chemical weathering profiles under open- and closed-system conditions, representing partially and fully water-saturated regolith, respectively. Under open-system conditions, equilibrium bicarbonate concentrations vary as a power-law function of $pCO_2$ ($y = kx^n$) where $n$ is dependent on reaction stoichiometry and $k$ is dependent on both reaction stoichiometry and the equilibrium constant. Under closed-system conditions, bicarbonate concentrations vary linearly with $pCO_2$ at low values and approach open-system scaling at high $pCO_2$. To describe the potential role of thermodynamic limitations in the global silicate weathering feedback, we develop a new mathematical framework to assess weathering feedback strength in terms of both (1) steady-state atmospheric $pCO_2$ concentrations, and (2) susceptibility to secular changes in degassing rates and transient carbon cycle perturbations, which we term 1st and 2nd order feedback strength, respectively. Finally, we discuss the implications of these results for the effects of vascular land plant evolution on feedback strength, the potential role of vegetation in controlling modern solute fluxes, and the application of these frameworks to a more complete functional description of the silicate weathering feedback. Most notably, the dependence of equilibrium solute concentrations on $pCO_2$ may represent a direct weathering feedback largely independent of climate and modulated by belowground organic carbon respiration.

© 2018 Elsevier B.V. All rights reserved.

## 1. Introduction

The stability of global temperatures within the range of planetary habitability over 4 billion years requires a tightly coupled negative feedback system within the carbon cycle to regulate atmospheric greenhouse gas concentrations (Urey, 1952). This feedback system is thought to be the drawdown of atmospheric $CO_2$ by terrestrial silicate weathering coupled with oceanic carbonate deposition (Walker et al., 1981), potentially modulated by the net oxidation and burial of organic carbon (Petsch et al., 2000; France-Lanord and Derry, 1997) and sulfide minerals (Torres et al., 2014). In this framework, weathering rates dynamically balance tectonic degassing rates and net organic carbon burial and oxidation, as well as transient carbon cycle perturbations. During transient (<1 Ma) carbon cycle perturbations, silicate weathering also sets the recovery timescale of the ocean–atmosphere system through the rate at which excess $CO_2$ is sequestered or deficit $CO_2$ is replenished (Sundquist, 1991; Archer, 2005). Although many previous studies have characterized the mathematical form of the silicate weathering feedback as a function of $CO_2$, these have historically focused on the dependence of mineral dissolution kinetics on $CO_2$ concentrations and temperatures (*e.g.* Walker et al., 1981; Berner et al., 1983; Velbel, 1993; Kump et al., 2000; West, 2012). In contrast, recent work has suggested that thermodynamic limitations to weathering act as a first-order component of the silicate weathering feedback (Maher and Chamberlain, 2014) and may in turn vary as a function of $CO_2$ in the weathering environment (Calmels et al., 2014).

* Corresponding author at: 450 Serra Mall Bldg. 320, Stanford, CA, 94305, USA.
*E-mail address:* mwinnick@stanford.edu (M.J. Winnick).

https://doi.org/10.1016/j.epsl.2018.01.005
0012-821X/© 2018 Elsevier B.V. All rights reserved.

Thermodynamic limitations to weathering describe the approach to a metastable equilibrium involving dissolving minerals and precipitating secondary phases. When residence times of subsurface waters are greater than the time needed to reach this metastable equilibrium, solute concentrations remain constant over a wide range of discharge values. Under these conditions, solute fluxes become linearly dependent on discharge (Maher, 2011) resulting in 'chemostatic' behavior. In terms of the silicate weathering feedback, the thermodynamic limit can be thought of as the maximum potential weathering rate for given environmental (*i.e.* temperature, runoff, vegetation) and lithological boundary conditions. Additionally, the widespread observation of near-chemostatic behavior across small (Godsey et al., 2009; $HCO_3^-$ *log–log* slopes of −0.05 to −0.15) and major river systems (Moon et al., 2014; median $HCO_3^-$ *log–log* slope of −0.16) suggest that thermodynamic limitations may play an important role in controlling riverine solute fluxes. Here, we explore the relationships between $CO_2$ in the weathering zone, thermodynamic limits on solute concentrations, and the role of such limits in governing the strength of the silicate weathering negative feedback.

The concept of silicate weathering feedback strength has been present in the literature since the 1980s and has been used to describe multiple phenomena. These include both (1) the role of weathering in setting steady-state atmospheric $pCO_2$ for a given volcanic degassing rate; and (2) the response of atmospheric $pCO_2$ to perturbations in the carbon cycle, such as secular changes in degassing rates and transient carbon release events. The first of these effects arises from the fact that, due to the relatively small reservoir size of the atmosphere–ocean system ($\sim 3 \times 10^{18}$ mol C) compared to the magnitude of the input and removal fluxes of carbon ($\sim 8 \times 10^{18}$ mol C $My^{-1}$) (Gaillardet et al., 1999), weathering fluxes must balance tectonic degassing and organic carbon burial/oxidation on timescales of $>10^5$ yrs in order to maintain habitable conditions (Berner and Caldeira, 1997; Caves et al., 2016). Accordingly, steady-state atmospheric $pCO_2$ is determined by the value at which weathering fluxes equal degassing fluxes. The second effect refers to the sensitivity of weathering fluxes to changes in atmospheric $pCO_2$ and controls both the response of steady-state $pCO_2$ to a change in secular degassing rates and the recovery timescale in response to transient carbon release events (Sundquist 1991; Archer, 2005; Uchickawa and Zeebe, 2008). Despite these effects being described throughout the literature, there has as yet been no formal classification for these effects as separate, though related, phenomena.

Herein, we present mathematical frameworks for quantifying the dependence of equilibrium solute concentrations on $pCO_2$ and for assessing the strength of the silicate weathering feedback in terms of driving both steady-state atmospheric $pCO_2$ and the sensitivity of atmospheric $pCO_2$ to carbon cycle perturbations. Theoretical arguments are supported by reactive transport simulations of weathering profiles. Finally, we discuss the implications of these theoretical arguments for the silicate weathering effects caused by the rise and spread of vascular land plants, the role of plant productivity in controlling modern weathering fluxes, and the potential role of thermodynamic limits as a direct feedback between weathering rates and atmospheric $CO_2$ concentrations independent of climate.

## 2. Mathematical framework

### 2.1. First v. second order silicate weathering feedback strength

In order to examine the effects of thermodynamic limitations on the global silicate weathering feedback, we first develop a mathematical framework to assess feedback strength. Although the silicate weathering negative feedback system has been described extensively in the literature, descriptions of feedback strength have historically referred to two separate phenomena. Specifically, the strength of the negative feedback has been used to describe both (1) steady-state atmospheric $pCO_2$ given tectonic degassing and organic burial/oxidation rates (*e.g.* Berner et al., 1983; Caves et al., 2016); and (2) the response of atmospheric $pCO_2$ to perturbations in degassing and organic carbon burial/oxidation rates (*e.g.* Sundquist, 1991; Archer, 2005; Uchikawa and Zeebe, 2008).

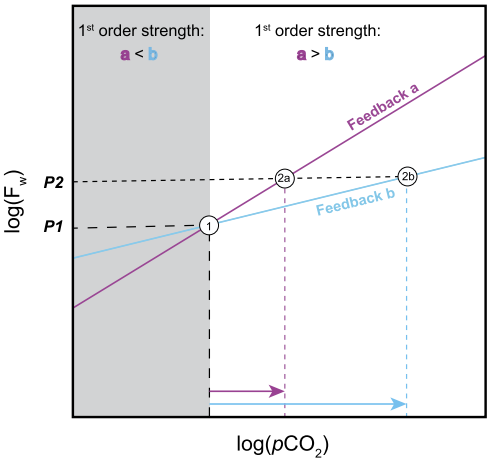



**Fig. 1.** Conceptual diagram of 1st and 2nd order silicate weathering feedback strengths for two functional forms of the feedback, Feedbacks a and b. Gray and white shaded areas indicate relative 1st order feedback strength. Colored arrows denote the response of $pCO_2$ to long-term changes in degassing rates from P1 to P2.

As demonstrated in previous studies, steady-state atmospheric $pCO_2$ is set by the functional dependence of chemical weathering rates on atmospheric $pCO_2$ as conceptualized in Fig. 1. At any given $CO_2$ production rate ($P$) representing $CO_2$ degassing, atmospheric $pCO_2$ is set by the $pCO_2$ value at which the silicate weathering flux ($F_w$) is equal to $P$ (Berner et al., 1983; Caves et al., 2016). The weathering feedback is commonly represented in global carbon-cycle models as a power-law equation, approximating empirical dependencies of weathering rates on climatic variables (e.g. Walker et al., 1981; Berner, 1991; Uchikawa and Zeebe, 2008). Given the power-law functional form of the silicate weathering feedback,

$$F_w = k \cdot (pCO_2)^n, \tag{1}$$

steady-state atmospheric $pCO_2$ varies as a function of $k$ and $n$, which together represent global weatherability (Kump and Arthur, 1997; Kump et al., 2000). When the Earth system has a higher weatherability, for example due to more reactive surface lithology, steady-state atmospheric $pCO_2$ for a given degassing rate is lower and the strength of the weathering feedback is said to be higher. We define this aspect, based on the absolute value of weathering rates at a given $pCO_2$, as the 1st order feedback strength. This definition of feedback strength incorporates both $k$ and $n$ values as they combine to set the silicate weathering flux for a given $pCO_2$.

In Fig. 1, we demonstrate differences in 1st order feedback strength between two power-law feedback functions, as represented by the value of $F_w$ at any given $pCO_2$. At Point 1 where these weathering curves intersect, $F_w(pCO_2)$ is the same, indicating the same 1st order feedback strength. At lower $pCO_2$, Feedback *b* has a higher 1st order feedback strength (gray shading), and at higher $pCO_2$, Feedback *a* has a higher 1st order feedback strength.

The second feedback phenomenon refers to how susceptible the climate is to carbon cycle perturbations. This aspect of feedback strength is controlled by the slope of the weathering curve, which represents the sensitivity of weathering rates to changes in $pCO_2$.

Quantitatively, this sensitivity is calculated as the derivative of $F_w$ with respect to $pCO_2$ (Eq. (1)),

$$\frac{\partial F_w}{\delta(pCO_2)} = k \cdot n \cdot (pCO_2)^{n-1}. \quad (2)$$

As the derivative of the 1st order feedback strength, we term this phenomenon the 2nd order feedback strength. When the 2nd order feedback strength is higher, long-term changes in tectonic degassing rates result in smaller changes in steady-state atmospheric $pCO_2$, and transient carbon release events result in shorter recovery times to steady-state atmospheric $pCO_2$. Weathering rates that are more sensitive to $pCO_2$ (*i.e.* higher 2nd order feedback) will respond more strongly to a carbon release event, leading to faster removal of excess $CO_2$.

In Fig. 1, the concept of 2nd order feedback strength is demonstrated by the change in $pCO_2$ associated with an increase in long-term $pCO_2$ production ($P$). As represented by the higher slope in log–log space, Feedback *a* has a higher 2nd order feedback strength at Point 1. Therefore, with an increase in long-term production from P1 to P2, $\Delta pCO_2$ is larger for Feedback *b* due to its lower 2nd order feedback strength.

Although we define the 1st and 2nd order feedback strength in the context of the power-law functional form, this framework may be applied to any functional form of the relationship between silicate weathering rates and atmospheric $pCO_2$ in which 1st order strength represents the magnitude of the weathering curve and 2nd order strength represents the slope of the weathering curve. Whereas previous studies have alluded to both aspects of feedback strength, they are not commonly distinguished; and although they are directly related, they will not necessarily co-vary through Earth history. In other words, an Earth system with lower steady-state atmospheric $CO_2$ concentrations will not necessarily be less susceptible to perturbations depending on the functional form. The framework proposed here will be used to analyze how the $CO_2$ dependence of equilibrium solute concentrations affects the strength of the weathering feedback.

### 2.2. $CO_2$ dependence of equilibrium solute concentrations

In natural weathering systems, when fluid residence times are short relative to reaction rates, kinetic considerations largely govern the amount of solute released (Aagaard and Helgeson, 1982; Helgeson et al., 1984). However, as fluid residence times increase, the approach to thermodynamic equilibrium becomes an important component in the overall rate law (Aagaard and Helgeson, 1982; Steefel et al., 2015). At long fluid residence times, equilibrium solute concentrations set the flux of weathering products, resulting in a thermodynamic limit (Thompson, 1959; Bahr and Rubin, 1987; Knapp, 1989; Maher, 2011), also referred to as transport-limited weathering (Stallard and Edmond, 1983; Kump et al., 2000). Under these conditions, concentrations remain static across a wide range of stream discharge, and fluxes are linearly dependent on discharge rates. In terms of the silicate weathering feedback, thermodynamic limitations can be thought of as the maximum potential weathering rate for a given atmospheric $pCO_2$ and associated temperature, runoff, and vegetation conditions.

In this section, we develop a scaling relationship between equilibrium solute concentrations and weathering zone $pCO_2$ under both open- and closed-system weathering conditions, relating to near-saturated and saturated flow, respectively (*e.g.* Berner, 1992), which are compared to reactive transport simulations in Section 4. This framework, based on the law of mass action, is similar to that of Drever (1997) in scaling $[Ca^{2+}]$ with $pCO_2$ for carbonate weathering. The dependence of equilibrium concentrations on $CO_2$ results from the impact of $CO_2$ on solution pH and thus the thermodynamic driving forces for mineral dissolution/precipitation. We note that for the purposes of our discussion, scaling relationships are solved in terms of concentrations and $pCO_2$, and are compared to simulations that include activity/fugacity calculations. Additionally, we note that these relationships relate to the $pCO_2$ that waters experience in the subsurface weathering zone. The relationship between atmospheric and weathering zone $pCO_2$ is discussed in Section 5.

We start with a theoretical silicate weathering reaction in which a primary mineral ($M$) reacts with carbonic acid to form a secondary mineral ($S$), bicarbonate, cations, and silica:

$$mM + 2CO_2(g) + H_2O \leftrightarrow sS + 2HCO_3^- + aA + bB + cSiO_2(aq), \quad (3)$$

where lower case letters represent stoichiometric coefficients, and $A$ and $B$ represent divalent and monovalent cation weathering products, respectively. We note that the number of cation products and precipitating minerals may vary between reactions, though this general framework will still apply. Given this reaction, we then write the equilibrium constant ($K$) in terms of the equilibrium activities of reactants as,

$$K = \frac{[HCO_3^-]^2[A]^a[B]^b[C]^c}{(pCO_2)^2}. \quad (4)$$

Next, assuming that Eq. (3) is the only reaction operating to control solute concentrations and that stoichiometric ratios are therefore maintained between weathering products, we rewrite the cation and silica activities in terms of the activity of $HCO_3^-$ based on the stoichiometric balance in Eq. (3), for example in terms of $A$, as,

$$[A] = (a/2)\left[HCO_3^-\right]. \quad (5)$$

Substituting these equalities in place of cation and silica activities, we rewrite Eq. (4) as,

$$K = \frac{r \cdot [HCO_3^-]^{2+a+b+c}}{(pCO_2)^2}, \quad (6)$$

where $r$ represents the relative stoichiometric coefficients,

$$r = \left(\frac{a}{2}\right)^a \left(\frac{b}{2}\right)^b \left(\frac{c}{2}\right)^c. \quad (7)$$

Rearranging Eq. (6) so that $[HCO_3^-]$ is a function of $pCO_2$, we arrive at,

$$\left[HCO_3^-\right]_{eq} = \left(K \cdot r^{-1}\right)^{\frac{1}{2+a+b+c}} \cdot (pCO_{2(eq)})^{\frac{2}{2+a+b+c}}. \quad (8)$$

The $[HCO_3^-]_{eq}$ is then a function of $pCO_2$ in the functional form of $y = kx^n$, coincidentally similar to the functional form of Eq. (1) used in carbon cycle models to describe the silicate weathering feedback. Here, the coefficient $k$ is dependent on both the equilibrium constant and reaction stoichiometry and the exponent $n$ is dependent only on reaction stoichiometry. We note that this allows both the coefficient and the exponent of the $CO_2$-dependence of thermodynamic weathering limits to vary with changes in mineralogy, as discussed in detail in Sections 4 and 5. This generalized framework is then applicable across a range of acid-base weathering reactions.

We then apply this $CO_2$-dependence of $[HCO_3^-]_{eq}$ to two end-member weathering conditions: open-system and closed-system. Under open-system weathering conditions, $pCO_2$ of infiltrating waters is maintained at a constant value. This condition may be maintained through subsurface plant and microbial respiration and in abiotic systems through $CO_2$ diffusion rates from the atmosphere into the subsurface that keep pace with infiltration and reaction

rates. In the open system case, $pCO_2$ in Eq. (8) represents the $pCO_2$ of waters in equilibrium with atmospheric or soil $pCO_2$, and Eq. (8) may be used directly to scale $HCO_3^-$ fluxes with initial $pCO_2$.

Closed-system weathering, which describes a system in which $pCO_2$ is initially in equilibrium with atmospheric or soil $pCO_2$ and the reaction is subsequently run to equilibrium without additional $CO_2$ inputs, is more complex. Closed-system weathering in natural systems is associated with the inhibition of gas diffusion through saturated soil pores, limiting $CO_2$ diffusion from the atmosphere to the subsurface in abiotic and biotic systems, and additionally limiting microbial respiration rates through the suppression of $O_2$ diffusion into the subsurface in biotic systems. In this scenario, $pCO_2$ in Eq. (8) is constrained by the mass conservation of carbon in the system such that,

$$(pCO_2)_i = (pCO_2)_{eq} + h \cdot \left[HCO_3^-\right]_{eq}, \tag{9}$$

where $h$ is the solubility constant for $CO_2$ (*i.e.* Henry's constant, bar/M) to convert molar units of $[HCO_3^-]$ to its equivalent pressure, and subscripts $i$ and $eq$ denote initial and equilibrium values, respectively. This assumes a negligible amount of carbon in the form of $CO_3^{2-}$ and must be adjusted when applying to high-pH solutions. We note that this mass conservation condition applies to silicate weathering where the stoichiometric ratio of $CO_2$:$HCO_3^-$ is 1:1. For carbonate minerals, $(pCO_2)_i$ will equal $(pCO_2)_{eq} + 0.5 * h * [HCO_3^-]$ due to the release of rock carbon. This mass balance can be substituted into Eq. (8) to solve for the dependence of $[HCO_3^-]_{eq}$ on $(pCO_2)_i$ as,

$$\left[HCO_3^-\right]_{eq} = \left(K \cdot r^{-1}\right)^{\frac{1}{2+a+b+c}} \cdot \left((pCO_2)_i - h \cdot \left[HCO_3^-\right]_{eq}\right)^{\frac{2}{2+a+b+c}}. \tag{10}$$

The sensitivity of $HCO_3^-$ fluxes to initial $pCO_2$ of infiltrating waters in a closed system is therefore highly non-linear and does not follow the simple power-law scaling of Eq. (8). As we demonstrate in Section 4, this functional form causes preferential partitioning of carbon into $(pCO_2)_{eq}$ with increasing $(pCO_2)_i$ due to the greater exponent in the numerator relative to the denominator in Eq. (6). The result of this is an evolution of the scaling relationship between $[HCO_3^-]$ and initial $pCO_2$ from near-linear at low $pCO_{2(i)}$, to that approaching the open-system scaling of Eq. (8) at high $pCO_{2(i)}$.

In this study, our analysis focuses on the dissolution of plagioclase feldspar ($An_{20}$) and precipitation of halloysite, represented by,

$$1.66Ca_{0.2}Na_{0.8}Al_{1.2}Si_{2.8}O_8 + 2CO_2(g) + 3H_2O \leftrightarrow Al_2Si_2O_5(OH)_4 + 0.33Ca^{2+} + 1.33Na^+ + 2.66SiO_2(aq) + 2HCO_3^-, \tag{11}$$

where the equilibrium constant at 15 °C is $10^{-13.3}$, reflecting the equilibrium constants for plagioclase dissolution, $CO_2$ solubility, carbonic acid dissociation, and halloysite precipitation (Wolery et al., 1990; Arnorsson and Stefansson, 1999). Plugging these values into Eq. (8), we arrive at an open-system scaling relationship of,

$$\left[HCO_3^-\right]_{eq} = 0.0084(pCO_2)_i^{0.316}, \tag{12}$$

where activities are represented by concentrations in molar units. Similarly, we plug values from Eq. (11) into Eq. (10) to calculate a closed-system scaling relationship of,

$$\left[HCO_3^-\right]_{eq} = 0.0084\left((pCO_2)_i - 22.2\left[HCO_3^-\right]_{eq}\right)^{0.316}. \tag{13}$$

As the original scaling relationship is calculated based on $CO_2$(g), we use a coefficient of $CO_2$ solubility of 22.2 bars/M at 15 °C to convert $HCO_3^-$ activity units to the equivalent partial pressure units. Due to the non-linear nature of this equation, we developed and use a uni-directional root-solving algorithm with a solution threshold of $10^{-6}$ to calculate $[HCO_3^-]$ at a given $pCO_2$ (Supplemental Materials).

Additionally, the precipitation of other low solubility minerals often adds complexity to these relationships. For example, we also show the effects of allowing for amorphous silica ($SiO_2$(am)) precipitation when $SiO_2$(aq) activities reach $SiO_2$(am) saturation. The full derivation of this relationship is provided in the Supplemental Materials. Mathematically, when $SiO_2$(aq) reaches $SiO_2$(am) saturation, Eq. (9) for open-system scaling of plagioclase dissolution and halloysite and $SiO_2$(am) precipitation becomes,

$$\left[HCO_3^-\right]_{eq} = 0.038 * (pCO_2)_{eq}^{0.545}. \tag{14}$$

Lastly, although our analysis focuses on the reaction represented by Eq. (11), for simplicity we note that this framework is applicable to a wide range of reactions. We include scaling relationships for dissolution of plagioclase across the anorthite–albite solid solution series and sanidine, and for halloysite, kaolinite, and amorphous silica precipitation in Table 1 and Fig. 3.

## 3. Reactive transport methods

The reactive transport model (RTM) CrunchFlow (Steefel et al., 2015) was used to simulate 1-D weathering profiles. Following the methods of Maher (2011), profiles were initialized with a granitic composition of 18.2% wt. each of plagioclase feldspar (20% mol anorthite) and K-feldspar, 60.6% wt. quartz, and 3% wt. halloysite. This mineral assemblage is meant to broadly represent continental granites, though we note that granites display a large degree of variability in cation content. Initial porosity is 17%. Halloysite was chosen as the dominant secondary mineral based on comparisons of simulated equilibrium concentrations of $SiO_2$(aq) and $[Na^+]/[H^+]$ to granitic catchment solute data (Maher and Chamberlain, 2014). Feldspar mineral surface areas were set to 0.1 $m^2/g$ within the range of observations (White and Brantley, 2003). Dissolution rate constants and activation energies were taken from a compilation by Palandri and Kharaka (2004). We assume no direct dependence of kinetic rates on the $CO_2$(aq) concentrations (*e.g.* Navarre-Sitchler and Thyne, 2007) as the focus of the study is the steady-state solute concentrations. We use equilibrium constants primarily from the EQ3/EQ6 thermodynamic database (Wolery et al., 1990) for minerals and aqueous complexes, and equilibrium constants for plagioclase solid solution series dissolution from Arnorsson and Stefansson (1999).

We simulate both open- and closed-system weathering scenarios as defined in Section 2.2. Open-system weathering is simulated by specifying unsaturated conditions (0.75% saturation) and constant water flux, as well as high gas fluxes into the domain that keep pace with infiltration and reaction rates. Closed-system weathering is simulated by specifying saturated conditions and no gas flux into the domain. Under these scenarios, we generate a suite of simulations across $pCO_2$ values ranging from $10^2$–$10^6$ ppm. Simulations are run at 15 °C with infiltration fluxes of 0.5–10 m/yr; however due to the lack of dependence of results on flow rate, we display results from 0.5 m/yr flux simulations in summary figures. Fluid travel times are computed as $L\theta/q$ where $L$ is the depth, $\theta$ is the water content and $q$ is the infiltration flux. Simulations were run to a quasi-steady state such that aqueous concentrations were constant across the domain over 100 yr timescales. The length of the domain was set to 25 m in order to allow the fluids to reach equilibrium with primary and secondary minerals such that the net reaction rate was zero. The final "equilibrium concentrations" are tabulated from these steady-state endpoints.

**Table 1**
Reaction stoichiometries, equilibrium constants, and $CO_2$ scaling parameters.

| Reaction | Formula | log($K$) @ 15 °C | | Coefficient ($k$) | | Exponent ($n$) |
|---|---|---|---|---|---|---|
| | | Halloysite precip. | Kaolinite precip. | Halloysite precip. | Kaolinite precip. | |
| Plag(An0) to Halloysite/Kaolinite | $2NaAlSi_3O_8 + 2CO_2(g) + 3H_2O \leftrightarrow Al_2Si_2O_5(OH)_4 + 2Na^+ + 4SiO_2(aq) + 2HCO_3^-$ | −20.54004 | −16.6796 | 0.001914168 | 0.005814803 | 0.25 |
| Plag(An20) to Halloysite/Kaolinite | $1.67Ca_{0.2}Na_{0.8}Al_{1.2}Si_{2.8}O_8 + 2CO_2(g) + 3H_2O \leftrightarrow Al_2Si_2O_5(OH)_4 + 0.33Ca^{2+} + 1.33Na^+ + 2.67SiO_2(aq) + 2HCO_3^-$ | −13.30149612 | −9.441056116 | 0.008384994 | 0.034154841 | 0.316 |
| Plag(An40) to Halloysite/Kaolinite | $1.43Ca_{0.4}Na_{0.}6Al_{1.4}Si_{2.6}O_8 + 2CO_2(g) + 3H_2O \leftrightarrow Al_2Si_2O_5(OH)_4 + 0.57Ca^{2+} + 0.86Na^+ + 1.71SiO_2(aq) + 2HCO_3^-$ | −8.4124 | −4.55196 | 0.031939582 | 0.180765286 | 0.39 |
| Plag(An60) to Halloysite/Kaolinite | $1.25Ca_{0.6}Na_{0.4}Al_{1.6}Si_{2.4}O_8 + 2CO_2(g) + 3H_2O \leftrightarrow Al_2Si_2O_5(OH)_4 + 0.75Ca^{2+} + 0.5Na^+ + SiO_2(aq) + 2HCO_3^-$ | −4.556425 | −0.695985 | 0.139894684 | 1.129807913 | 0.47 |
| Plag(An80) to Halloysite/Kaolinite | $1.11Ca_{0.8}Na_{0.2}Al_{1.8}Si_{2.2}O_8 + 2CO_2(g) + 3H_2O \leftrightarrow Al_2Si_2O_5(OH)_4 + 0.88Ca^{2+} + 0.22Na^+ + 0.44SiO_2(aq) + 2HCO_3^-$ | −1.783618801 | 2.076821199 | 0.533395427 | 6.512731115 | 0.563 |
| Plag(An100) to Halloysite/Kaolinite | $CaAl_2Si_2O_8 + 2CO_2(g) + 3H_2O \leftrightarrow Al_2Si_2O_5(OH)_4 + Ca^{2+} + 2HCO_3^-$ | 0.23037 | 4.09081 | 1.503910178 | 29.15269027 | 0.667 |
| Sanidine to Halloysite/Kaolinite | $2KAlSi_3O_8 + 2CO_2(g) + 3H_2O \leftrightarrow Al_2Si_2O_5(OH)_4 + 2K^+ + 4SiO_2(aq) + 2HCO_3^-$ | −25.0773 | −21.21686 | 0.000518588 | 0.001575352 | 0.25 |
| Plag(An0) to $SiO_2$(am) and Halloysite/Kaolinite | $2NaAlSi_3Os + 2CO_2(g) + 3H_2O \leftrightarrow Al_2Si_2O_5(OH)_4 + 4SiO_2(am) + 2Na^+ + 2HCO_3^-$ | −9.029 | −5.16856 | 0.005530317 | 0.051034046 | 0.5 |
| Plag(An20) to $SiO_2$(am) and Halloysite/Kaolinite | $L67Ca_{0.2}Na_{0.8}Al_{1.2}Si_{2.8}O_8 + 2CO_2(g) + 3H_2O \leftrightarrow Al_2Si_2O_5(OH)_4 + 2.67SiO_2(am) + 0.33Ca^{2+} + 1.33Na^+ + 2HCO_3^-$ | −5.686 | −1.8261828 | 0.038478585 | 0.433530122 | 0.545 |
| Plag(An40) to $SiO_2$(am) and Halloysite/Kaolinite | $1.43Ca_{0.4}Na_{0.6}Al_{1.4}Si_{2.6}O_8 + 2CO_2(g) + 3H_2O \leftrightarrow Al_2Si_2O_5(OH)_4 + 1.71SiO_2(am) + 0.57Ca^{2+} + 0.86Na^+ + 2HCO_3^-$ | −3.4914304 | 0.3690096 | 0.146121487 | 1.949989817 | 0.583 |
| Plag(An60) to SiO2(am) and Halloysite/Kaolinite | $1.25Ca_{0.6}Na_{0.4}Al_{1.6}Si_{2.4}O_8 + 2CO_2(g) + 3H_2O \leftrightarrow Al_2Si_2O_5(OH)_4 + SiO_2(am) + 0.75Ca^{2+} + 0.5Na^+ + 2HCO_3^-$ | −1.678665 | 2.181775 | 0.472733386 | 7.272798833 | 0.615 |
| Plag(An80) to $SiO_2$(am) and Halloysite/Kaolinite | $1.11Ca_{0.8}Na_{0.2}Al_{1.8}Si_{2.2}O_8 + 2CO_2(g) + 3H_2O \leftrightarrow Al_2Si_2O_5(OH)_4 + 0.44SiO_2(am) + 0.88Ca^{2+} + 0.22Na^+ + 2HCO_3^-$ | −0.4783156 | 3.3821244 | 1.034844341 | 17.95048838 | 0.642 |
| Sanidine to $SiO_2$(am) and Halloysite/Kaolinite | $2KAlSi_3O_8 + 2CO_2(g) + 3H_2O \leftrightarrow Al_2Si_2O_5(OH)_4 + 4SiO_2(am) + 2K^+ + 2HCO_3^-$ | −13.56626 | −9.70582 | 0.000405915 | 0.003745804 | 0.5 |

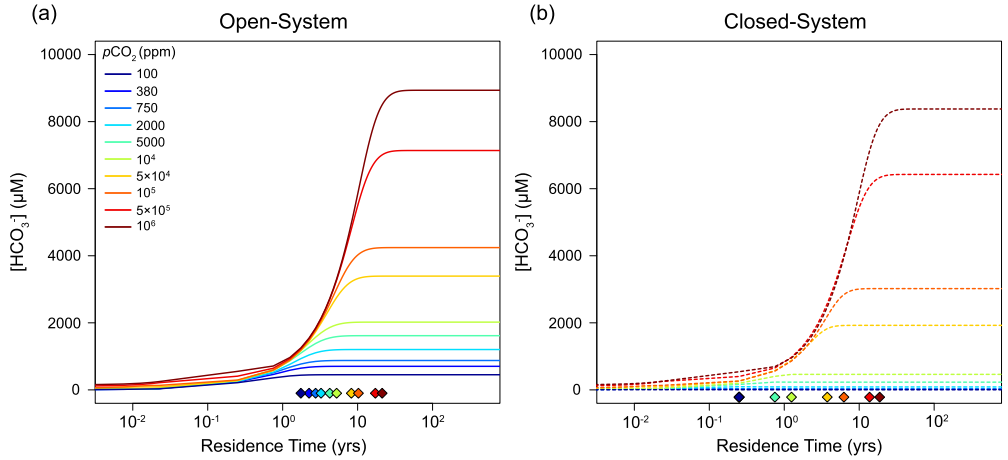



**Fig. 2.** Semi-log plots of $[HCO_3^-]$ temporal evolution from CrunchFlow weathering profile simulations for (a) open-system weathering; and (b) closed-system weathering. Line colors denote initial $pCO_2$ of infiltrating waters, and diamonds denote the residence time at which concentrations reach 95% of equilibrium values. (For interpretation of the colors in this figure, the reader is referred to the web version of this article.)

## 4. Results

Crunchflow RTM simulations demonstrate the effects of $pCO_2$ on the approach to equilibrium as fluids infiltrate through a weathering profile. Weathering profile simulations for open- and closed-system scenarios are shown in Fig. 2, with $[HCO_3^-]$ plotted against residence times for the range of initial $pCO_2$. These solute evolution curves display increasing $[HCO_3^-]$ with increasing residence time, with values plateauing when concentrations reach equilibrium between the dissolving and precipitating phases. In both open- and closed-system scenarios, $[HCO_3^-]_{eq}$ increases with increasing $pCO_2$. In the open-system scenario, $[HCO_3^-]_{eq}$ ranges from 450 μM at $pCO_2$ of $10^{-4}$ bars to 8935 μM at $pCO_2$ of 1 bar. In the closed system scenario, equilibrium concentrations range from 4.8 μM at $pCO_2$ of $10^{-4}$ bars to 8377 μM at $pCO_2$ of 1 bar. In all cases, $[HCO_3^-]_{eq}$ is lower under closed-system conditions for a given $pCO_2$ than under open-system conditions. As a result, waters require more time to reach $[HCO_3^-]_{eq}$ under open-system weathering, as denoted by the colored diamonds in Fig. 2. We also note that the range of equilibrium timescales shown in Fig. 2 is comparable to simulated median groundwater residence times for water-

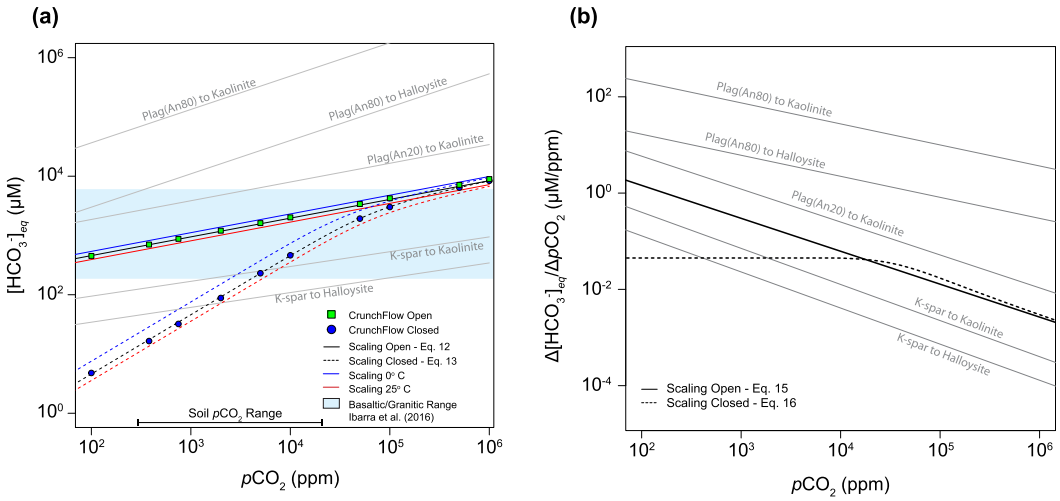



**Fig. 3.** (a) Comparison of $[HCO_3^-]_{eq}$ v. $pCO_2$ (log–log) between CrunchFlow simulations and scaling equations for open- and closed-system weathering relationships of Plagioclase(An20) to Halloysite. The blue shaded region represents the range of observed $[HCO_3^-]_{eq}$ in granitic and basaltic catchments from Ibarra et al. (2016), and typical soil $pCO_2$ values are noted at the bottom. The colored lines demonstrate temperature sensitivity of scaling at 0 °C (blue) and 25 °C (red), and gray lines represent open-system scaling relationships for additional reactions listed in Table 1. These curves also represent the 1st order feedback strength of the thermodynamic limits when scaled to global fluxes. (b) Sensitivity of $[HCO_3^-]_{eq}$ to changes in $pCO_2$ (log–log) calculated as the derivative of scaling relationships (e.g. Eqs. (15) and (16)). Curves correspond to the same reaction networks as in (a), and represent the 2nd order feedback strength of thermodynamic limits when scaled to global fluxes. (For interpretation of the colors in this figure, the reader is referred to the web version of this article.)

sheds in the United States (Maxwell et al., 2016). Additional solute evolution curves are provided for $[Ca^{2+}]$, $[Na^+]$, $[SiO_2]$, and pH in Supplementary Figs. 1 and 2.

Although RTM simulations are constrained by the thermodynamic relationships with which we develop scaling relationships in Section 2.2, a comparison of RTM simulations with Eqs. (12) and (13) allow us to examine the potential confounding effects of pH-dependent carbonate and aluminum speciation, ionic strength, and more complex mineral assemblages – all of which are encapsulated in CrunchFlow. Fig. 3a shows the relationship between $[HCO_3^-]_{eq}$ and $(pCO_2)_i$ for both open- and closed-system simulations in log–log space. Closed- and open-system simulation values converge at high $pCO_2$ in log–log space. The framework proposed in Section 2.2 is used to predict $[HCO_3^-]_{eq}$ from $pCO_2$, assuming the dominant reaction given the prescribed mineral assemblage is represented by Eq. (11). We then use Eqs. (12) and (13) for open- and closed-system scaling, respectively, to compare with CrunchFlow simulations (Fig. 3).

Our theoretical scaling relationships closely match CrunchFlow output despite a more rigorous representation of the carbonate and aluminum speciation dynamics, ionic strength effects, and transport dynamics in the model. Most notably, they capture the evolution of closed-system scaling from linear at low $pCO_2$ to that approaching open-system scaling at high $pCO_2$. Additionally, the agreement between Eqs. (8) and (10) and the RTM output, despite the presence of K-feldspar, suggests that scaling relationships will follow the behavior of the most soluble mineral. In field environments, there are additional processes within the weathering environment that may consume or produce protons such as reactions with organic matter. These processes have been included in previous studies, for example, via a coefficient that converts solute pH to protons available for primary mineral dissolution (Brantley et al., 2008). The role of these processes may potentially be evaluated in real-world systems through comparisons of measured pH, $pCO_2$, and $HCO_3^-$. While the inclusion of these complex reaction networks is beyond the scope of the current study, application of these equations to field environments must account for these processes.

For a comparison to environmental observations, we include the range of maximum riverine $[HCO_3^-]$ (interpreted as $[HCO_3^-]_{eq}$) from basaltic and granitic catchment systems evaluated by Ibarra et al. (2016) in Fig. 3a (blue shading) as well as typical soil $pCO_2$ ranges (400–20,000 ppm). Observed $[HCO_3^-]_{eq}$ ranges from 291–5920 μM with basaltic and granitic mean values of 1080 μM and 845 μM, respectively (Ibarra et al., 2016). These values fall within the range of open-system values of Plagioclase ($An_{20}$) and at the upper end of closed-system values for reasonable soil $pCO_2$ values. This comparison supports the general applicability of our mineral assemblage as a reasonable representation of real-world processes, though validation of our model against catchment data would require specific known reaction networks and hydrologic conditions (balance of open- v. closed-system weathering).

Fig. 3a also displays temperature sensitivity of Eqs. (12) and (13) for 0 °C and 25 °C. Lower temperatures result in higher $[HCO_3^-]_{eq}$ for a given $pCO_2$ due to higher equilibrium constants and higher $CO_2$ solubility. Additionally shown in Fig. 3a are open-system scaling relationships for plagioclase ($An_{80}$) and K-feldspar dissolution along with halloysite and kaolinite precipitation with equation parameters from Table 1.

Assuming that thermodynamics are the primary operative weathering feedback process (discussed further in Section 5.3), Fig. 3a can be thought of as a representation of 1st order feedback strength for different lithologies, scaled by runoff fluxes and lithological surface area. To examine the general characteristics of the sensitivity of thermodynamic limits to changes in $pCO_2$ (2nd order feedback strength) we plot the slopes of Fig. 3a weathering curves in Fig. 3b. These are generated by calculating the derivative, for example, of Eqs. (12) and (13) as,

$$\frac{d[HCO_3^-]}{d[pCO_2]} = 0.00281[pCO_2]^{-0.684}, \tag{15}$$

and,

$$\frac{d[HCO_3^-]}{d[pCO_2]} = 0.0028\left[\left([pCO_2] - 22.2\left[HCO_3^-\right]\right)^{0.684} + 0.0624\right]^{-1} \tag{16}$$

In log–log space, the sensitivity of open-system weathering to $pCO_2$ decreases linearly with increasing $pCO_2$, equivalent to decreasing 2nd order feedback strength. The 2nd order closed-system feedback strength remains roughly constant until $pCO_2 > 10^4$ ppm,

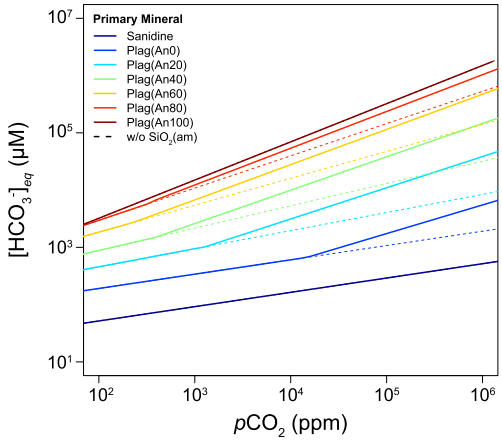



**Fig. 4.** The effects of $SiO_2$(am) precipitation on open-system scaling relationships for plagioclase weathering. Colored lines represent primary minerals across the albite-anorthite solid solution series as well as sanidine, and dashed lines represent scaling without $SiO_2$(am) precipitation. Scaling parameters from Table 1. (For interpretation of the colors in this figure, the reader is referred to the web version of this article.)

after which values decrease roughly linearly. As shown, closed-system weathering has a lower 2nd order feedback strength until roughly $2 \times 10^4$ ppm, above which it approaches open-system 2nd order feedback strength.

Lastly, we demonstrate the effects of allowing precipitation of $SiO_2$(am) in Fig. 4. Here the transition between scaling equations (e.g. Eqs. (12) and (14)) occurs when $SiO_2$(aq) reaches $SiO_2$(am) saturation. This is shown across the plagioclase anorthite-albite solid solution series, where the approach to $SiO_2$(am) saturation represents a balance of primary mineral solubility and the stoichiometric amount of $SiO_2$(aq) released during weathering. As shown in Table 1, as the stoichiometric amount of $SiO_2$(aq) released during weathering decreases from albite to anorthite, the change in the exponent $n$ with $SiO_2$(am) precipitation decreases.

## 5. Discussion

### 5.1. Stoichiometric controls on $CO_2$ dependence

As demonstrated in the preceding sections, the power-law dependence of equilibrium $[HCO_3^-]$ on $pCO_2$ during silicate weathering reactions is governed by a combination of mineral solubility and reaction stoichiometry. Specifically, within the power-law equation $y = kx^n$, the coefficient $k$ represents a combination of reaction stoichiometry and the equilibrium constant, whereas the exponent $n$ is simply the stoichiometric ratio of $CO_2$ to the sum of the reaction products. Although our analysis focuses primarily on the dissolution of plagioclase ($An_{20}$) and precipitation of halloysite and amorphous silica as a model system, these relationships allow us to examine the controls of reaction stoichiometry on $k$ and $n$ more generally.

For example, these relationships dictate that $n$ will increase as the stoichiometric sum of aqueous reaction products (*i.e.* cations and aqueous silica) decreases (Eq. (8)). Higher $n$ values, in turn, lead to a greater increase in $[HCO_3^-]_{eq}$ for a given change in $pCO_2$, as shown in Fig. 3. In terms of lithological controls, a shift to more basaltic minerals with an increasing proportion of divalent-($Ca^{2+}$) relative to monovalent-($Na^+$, $K^+$) cations in primary minerals causes $n$ to increase as shown in Table 1. This relationship arises from necessity of charge balance: less $Ca^{2+}$ is needed to balance $HCO_3^-$ anions as compared to $Na^+$. In the absence of $SiO_2$(aq) release during weathering, $n$ has the potential in Eq. (8) to vary from 0.5 ($n = 2/(2+2)$) in the case of albitic plagioclase to 0.667 ($n = 2/(2+1)$) in the case of anorthitic plagioclase. This variability is shown in Table 1 where $SiO_2$(am) precipitation is prescribed; however, when $SiO_2$(am) precipitation does not occur, $n$ may be lower than this range. In terms of global weathering fluxes, this increased sensitivity provides an additional mechanism by which lithology may control the weathering feedback. Previous studies suggest that the spatial coverage of basalt minerals increases the strength of the weathering feedback due to faster dissolution rates and greater solubility (Louvat and Allègre, 1997; Kump and Arthur, 1997; Dessert et al., 2003; Ibarra et al., 2016). Our analysis suggests that these effects also amplify the weathering feedback due to the higher sensitivity of mafic mineral weathering to changes in $pCO_2$ as a result of higher $n$ values.

This increased sensitivity of weathering to $pCO_2$ is also controlled by the nature of secondary mineral precipitation, which additionally acts to decrease the stoichiometric sum of aqueous reaction products. For example, the precipitation of $SiO_2$(am) at saturation causes an immediate increase in the sensitivity of $[HCO_3^-]$ to $pCO_2$ (Fig. 4, Table 1) by limiting the buildup of $SiO_2$(aq) in solution. This same logic applies to the precipitation of cation-rich clays and carbonates, solution ionic strength, and outside inputs of dissolved solids, including atmospheric deposition and plant-related inputs, that all act to alter the activity of solutes in the weathering environment.

As demonstrated in Section 2.2, reaction stoichiometry also affects the coefficient $k$ in a similar manner. However, $k$ is primarily dependent on the equilibrium constant for the net reaction, which can vary by many orders of magnitude (Table 1). For example, kaolinite and halloysite precipitation have the same stoichiometries but different equilibrium constants. Taken together, these results suggest the importance of reaction stoichiometry in controlling the sensitivity of weathering to subsurface $pCO_2$. Additionally, the importance of reaction stoichiometry in controlling the relationship between weathering potential and $pCO_2$ may allow for more accurate calculations of chemical denudation rates (Bouchez and Gaillardet, 2014), soil conditions, and sensitivity of weathering rates to environmental change through the measurement of solute concentrations in surface waters.

### 5.2. Geobiologic controls on weathering

In terms of weathering environment conditions, soil $pCO_2$ is controlled by a combination of atmospheric $pCO_2$ ($pCO_{2,atm}$), soil respiration rates ($SR$), and soil diffusivity ($D^*$) as,

$$pCO_{2_{soil}} = \frac{SR}{D^*}\left(L \cdot z - \frac{z^2}{2}\right) + pCO_{2_{atm}}, \tag{17}$$

where $L$ is the soil length scale and $z$ is depth (Cerling, 1984). Diffusivity is largely controlled by soil moisture and temperature, which influences soil $pCO_2$ responses to climate change (Goddéris et al., 2013). Soil respiration rates in turn are largely controlled by plant productivity, where $SR$ must balance net primary productivity (NPP) under steady-state conditions. As such, primary productivity may act as a first order control on equilibrium solute concentrations in modern catchment systems, as previously suggested for carbonate weathering across an elevation gradient (Calmels et al., 2014). This relationship allows for the generation and testing of hypotheses relating to the controls of vegetation and hydrology on weathering dynamics.

For example, it has been hypothesized that weathering rates are limited in humid environments by the availability of reactive gases ($CO_2$, $O_2$) and in arid environments by the availability of water (Li et al., 2017). However, this hypothesis is complicated by the non-linear relationship between soil respiration and subsurface hydrology: heterotrophic respiration and subsequent subsurface $pCO_2$ are limited under both low and high soil moisture conditions (*e.g.*

Davidson et al., 2012) that correspond to open- and closed-system end-members. Instead, we suggest that chemical weathering is optimized under moderate soil moisture conditions when soil respiration rates are maximized. Additionally, our analysis suggests chemical weathering is optimized in regions where chemical reaction fronts of dissolving minerals overlap with soil organic carbon and zones of active respiration that together facilitate high $pCO_2$ and open-system conditions. Hydrology also alters these relationships by controlling the balance of open- and closed-system conditions (*e.g.* Moore et al., 2012), water table height, lateral flow velocities, and ultimately where waters intersect chemical reaction fronts in the subsurface (Brantley et al., 2017; Winnick et al., 2017). In terms of global weathering fluxes, these hypotheses stress the importance of both active uplift/erosion in supplying fresh minerals and high soil respiration rates, as supported by evidence of high weathering fluxes from floodplain environments of mountain systems with active mineral deposition and higher primary productivity (Lupker et al., 2012). Lastly, the framework presented here suggests that lithology controls the extent to which biological processes may increase weathering, with mafic minerals displaying a higher sensitivity to $pCO_2$ than felsic minerals (Fig. 3).

The geobiologic control of weathering via soil $pCO_2$ also has implications for understanding the role of terrestrial land plant evolution in controlling chemical weathering rates and global climate throughout Earth history. Specifically, the transition from abiotic to biotic processes in the weathering zone should result in a substantial shift in the relationship between atmospheric $pCO_2$ ($pCO_{2,atm}$) and $pCO_2$ in the weathering zone ($pCO_{2,wz}$) by facilitating soil respiration (Eq. (17)). This fundamental shift is generally tied to the rise and spread of vascular land plants (Berner, 1992; Kump et al., 2000), although studies have postulated that pre-vascular organisms may have enhanced weathering rates as well (Keller and Wood, 1993).

Within our framework, the development of organic-rich terrestrial soils that elevate $pCO_{2,wz}$ relative to $pCO_{2,atm}$ result in a higher 1st order feedback strength and lower steady-state $pCO_{2,atm}$ concentrations for a given degassing rate under both open- and closed-system scenarios, similar to Berner (1992). In terms of global climate, conditions would have cooled with decreasing $pCO_{2,atm}$, as postulated by previous studies, until $pCO_{2,wz}$, temperature, and runoff adjusted to balance of weathering rates with tectonic degassing. The effects on 2nd order feedback strength are more complex. Under closed-system conditions, 2nd order feedback strength would be unchanged under reasonable ranges of subsurface $pCO_2$ ($10^2 - 2 \times 10^4$ ppm) due to the near-linear relationship between $[HCO_3^-]$ and $pCO_2$ (Fig. 3b). Under open-system conditions, 2nd order feedback strength would actually decrease for a given $pCO_{2,atm}$ value with increasing $pCO_{2,wz}$. However, this result is misleading, as the associated increase in 1st order feedback strength would lead to lower steady-state $pCO_2$ values and a therefore similar 2nd order feedback strength, or weathering curve slope, for any given degassing rate.

Comparing our analyses to those of Berner (1992), which also investigated open- and closed-system functional forms of the weathering feedback, reveals significant differences in our conclusions. Specifically, Berner (1992) considered feedback strength to be a sole function of the exponent value ($n$), and argued that open-system weathering would result in higher steady-state $pCO_2$ and much larger variability under a barren Earth (lower 1st and 2nd order feedback strengths). Our work demonstrates that feedback strength is instead dependent on the whole functional form of the weathering feedback, and that due to higher thermodynamic limits on weathering fluxes, open-system weathering will always result in lower steady-state and generally in more stable atmospheric $pCO_2$ than closed-system weathering.

### 5.3. Towards mechanistic representations of feedback dynamics in carbon cycle models

The dependence of equilibrium solute concentrations on $CO_2$ via soil pH suggests that thermodynamic limitations may represent a direct feedback between weathering rates and atmospheric $pCO_2$, in contrast to indirect feedbacks mediated by the response of temperature, runoff, and plant productivity to $pCO_2$. As shown in Eq. (17) in Section 5.2, changes in atmospheric $pCO_2$ will be reflected in the weathering zone, assuming no changes in respiration and diffusivity, providing a link between atmospheric $pCO_2$ and chemical weathering potential.

Although $CO_2$ serves as the primary variable in global carbon cycle models such as GEOCARB (Berner, 1991), existing representations are largely empirical and do not incorporate thermodynamic forcing in any mechanistic sense. Walker et al. (1981), for example, parameterized global weathering rates as a function of $pCO_2$ based on kinetic dissolution experiments on feldspars, which showed that at high $CO_2$ pressures (1–10 bars), the dependence of the dissolution rate on $pCO_2$ follows a power-law function with an exponent of 0.3 (Lagache, 1965). This relationship, however, may not be applicable to typical environmental $pCO_2$. Volk (1987) later proposed a Michaelis–Menten-style formulation to incorporate $CO_2$-fertilization effects on plant productivity and associated weathering that was later simplified and incorporated into the GEOCARB models (Berner, 1991). These formulations are empirical, justified by comparisons to weathering fluxes from vegetated and non-vegetated Icelandic streams (Volk, 1987), and are highly limited by considerations of plant physiology and nutrient limitations.

The GEOCARB formulation of $CO_2$-enhanced weathering associated with increased productivity has subsequently been incorporated into other global carbon cycle models including COMBINE (Goddéris and Joachimski, 2004), GEOCLIM (Donnadieu et al., 2006), COPSE (Bergman et al., 2004), and RockGeM (Colbourn et al., 2013). These models all additionally include indirect $CO_2$-dependencies via ($a$) temperature terms that simulate Arrhenius-style controls on kinetic rates, and ($b$) runoff terms that empirically simulate thermodynamic effects through their control on riverine solute dilution but do not allow for changes in equilibrium concentrations as discussed in this paper. Although the explicit, distributed simulation of geochemical weathering reactions at global scales remains computationally prohibitive, we suggest that the relationships presented in this paper may be used to develop more mechanistically-based parameterizations of the global weathering feedback in carbon cycle models.

While beyond the scope of this paper, this parameterization may be incorporated into existing solute production frameworks that model chemical weathering fluxes and $CO_2$ sequestration rates as a function of subsurface water flow and chemical equilibration timescales (*e.g.*, Maher and Chamberlain, 2014; von Blanckenburg et al., 2015). Within such a framework, increases in atmospheric $pCO_2$ would result in an attendant shift in $[HCO_3^-]_{eq}$ depending on the prescribed lithology. The translation of variable $[HCO_3^-]_{eq}$ into changes in chemical weathering would then be dependent on weathering regime: when weathering occurs at or near equilibrium, shifts in $[HCO_3^-]_{eq}$ translate directly to shifts in weathering fluxes, and when weathering occurs far from equilibrium, shifts in $[HCO_3^-]_{eq}$ result in little or no change in weathering fluxes.

We demonstrate these differences conceptually in Fig. 5 by comparing theoretical concentration-discharge patterns for high- and low-$pCO_2$ weathering scenarios. In Fig. 5, the high- and low-$pCO_2$ curves differ only in their equilibrium concentrations. At low discharge when fluid residence times are high, solute concentrations are able to approach thermodynamic equilibrium and the effects of $pCO_2$ are maximized, corresponding to the large dif-

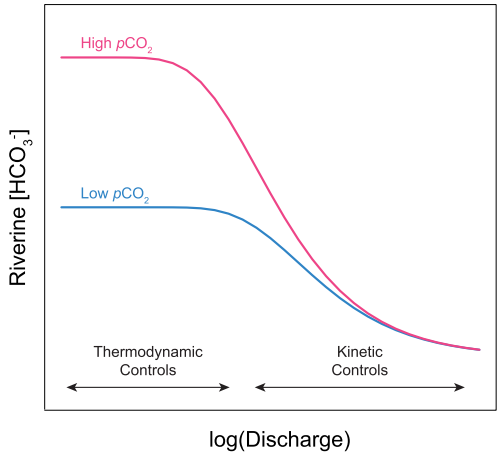



**Fig. 5.** Conceptual diagram of the effects of changing $pCO_2$ in the weathering environment on observed concentration-discharge relationships and weathering fluxes. At low discharge rates when fluids approach equilibrium solute concentrations, changes in $pCO_2$ translate directly into changing concentrations. At high discharge rates, when fluids are unable to approach equilibrium solute concentrations, kinetic rates control concentrations, and changes in $pCO_2$ have little to no effect on concentrations and weathering fluxes.

ference in concentrations. At high discharge when fluid residence times are reduced, kinetic rates become the primary control on solute concentrations, and changes in $pCO_2$ result in little or no change in weathering rates.

Despite the lack of constraints on how this feedback may be parameterized at the global scale, we can use this framework to describe general shifts in thermodynamic controls on feedback strength in response to Earth system evolution. For example, this mechanism allows feedback strength to change in response to lithological boundary conditions (*e.g.* Bluth and Kump, 1991; Ibarra et al., 2016) and uplift/erosional forcing (*e.g.* Raymo et al., 1988). Specifically, the parameters of Eqs. (8) and (10) change in response to reaction stoichiometry and equilibrium constants (Table 1), providing roles for both primary minerals and secondary phases in governing feedback strength. Additionally, uplift and erosion govern the availability of fresh mineral surface area, kinetic reaction rates, and the relative ability of infiltrating waters to reach equilibrium during subsurface transit (Maher and Chamberlain, 2014). This controls the ability of $pCO_2$ to affect weathering rates as shown in Fig. 5.

We can also make broad observations regarding the nature of silicate weathering feedback strength within our mathematical framework. One primary observation is that, assuming the silicate weathering feedback is non-linear (*i.e.* $n \neq 1$), the susceptibility of the climate system to changes in long-term secular degassing rates and short-term carbon cycle perturbations is dependent on background $pCO_2$. This is demonstrated clearly in Eq. (2) for a power-law functional form of the feedback, but is true of any derivative of a non-linear equation. If $n < 1$ as prescribed by a number of carbon cycle models (*e.g.* Walker et al., 1981; Berner, 1991; Sundquist, 1991; Zeebe, 2012), the climate system will be more susceptible to carbon cycle perturbations at higher $pCO_2$, resulting in larger changes in atmospheric $pCO_2$ with changes in secular degassing and longer steady-state recovery times during transient release events. This is evident from Fig. 3b, in which 2nd order feedback strength decreases with increasing $pCO_2$ under open-system conditions. Under this scenario, the climate system would take longer to recover from a carbon release event similar to that of the Paleocene–Eocene Thermal Maximum compared to a similar magnitude carbon release under modern climate conditions due to differences in initial $pCO_2$. This observation may provide a means with which to characterize the 2nd order feedback strength by comparing recovery timescales of well-studied Paleogene hyperthermal events in the context of overall declines in background atmospheric $pCO_2$.

## 6. Conclusions

The dependence of equilibrium solute concentrations on $CO_2$ conditions, as described and quantified in this study, acts as a fundamental control on maximum chemical weathering rates. As such, it may represent a direct feedback link between atmospheric $pCO_2$ and global weathering fluxes, acting to maintain planetary habitability independent of $CO_2$-modulated changes in climate and productivity. We also develop and apply a novel framework for assessing the feedback strength of silicate weathering as it relates to (1) setting steady-state atmospheric $pCO_2$ values for a given tectonic degassing rate; and (2) the sensitivity of $pCO_2$ and weathering fluxes to changes in degassing rates and transient carbon release events, respectively. Although we apply this framework solely to the power-law functional form of the feedback, it may be extended to include any functional form and used to better characterize 1st and 2nd order feedback strength through Earth history. Future work will need to parameterize these thermodynamic controls at local to global scales, particularly in terms of the respective roles of vegetation and the balance of saturated and unsaturated flow in determining maximum solute concentrations.

## Acknowledgements

We thank Daniel Ibarra, Jeremy Caves, Dana Thomas, Jérôme Gaillardet, and two anonymous reviewers for useful comments and suggestions that improved earlier versions of this manuscript. Funding to K.M. and M.W. was provided by the U.S. Department of Energy (DOE-DESC0014556) and the National Science Foundation (EAR-1254156).

## Appendix A. Supplementary material

Supplementary material related to this article can be found online at https://doi.org/10.1016/j.epsl.2018.01.005.

## References

Aagaard, P., Helgeson, H.C., 1982. Thermodynamic and kinetic constraints on reaction rates among minerals and aqueous solutions. I. Theoretical considerations. Am. J. Sci. 282, 237–285.
Archer, D., 2005. Fate of fossil fuel $CO_2$ in geologic time. J. Geophys. Res. 110, C09S05. https://doi.org/10.1029/2004JC002625.
Arnorsson, S., Stefansson, A., 1999. Assessment of feldspar solubility constants in water in the range 0 degrees to 350 degrees C at vapor saturation pressures. Am. J. Sci. 299 (3), 173–209.
Bahr, J.M., Rubin, J., 1987. Direct comparison of kinetic and equilibrium formulations for solute transport affected by surface reactions. Water Resour. Res. 23, 438–452.
Bergman, N.M., Lenton, T.M., Watson, A.J., 2004. COPSE: a new model of biogeochemical cycling over Phanerozoic time. Am. J. Sci. 304, 397–437.
Berner, R.A., Lasaga, A.C., Garrels, R.M., 1983. The carbonate–silicate geochemical cycle and its effect on atmospheric carbon dioxide over the past 100 million years. Am. J. Sci. 283, 641–683.
Berner, R.A., 1991. A model for atmospheric $CO_2$ over Phanerozoic time. Am. J. Sci. 291, 339–376.
Berner, R.A., 1992. Weathering, plants, and the long-term carbon cycle. Geochim. Cosmochim. Acta 56, 3225–3231.
Berner, R.A., Caldeira, K., 1997. The need for mass balance and feedback in the geochemical carbon cycle. Geology 25, 955–956.
von Blanckenburg, F., Bouchez, J., Ibarra, D.E., Maher, K., 2015. Stable runoff and weathering fluxes into the oceans over quaternary climate cycles. Nat. Geosci. 8 (7), 538–542.
Bluth, G.J.S., Kump, L.R., 1991. Phanerozoic paleogeology. Am. J. Sci. 291, 284–308.
Bouchez, J., Gaillardet, J., 2014. How accurate are rivers as gauges of chemical denudation of the Earth surface? Geology 42, 171–174.
Brantley, S.L., Bandstra, J., Moore, J., White, A.F., 2008. Modelling chemical depletion profiles in regolith. Geoderma 145, 494–504.

Brantley, S.L., Lebedeva, M.I., Balashov, V.N., Singha, K., Sullivan, P.L., Stinchcomb, G., 2017. Toward a conceptual model relating chemical reaction fronts to water flow paths in hills. Geomorphology 277, 100–117.

Calmels, D., Gaillardet, J., Francois, L., 2014. Sensitivity of carbonate weathering to soil $CO_2$ production by biological activity along a temperate climate transect. Chem. Geol. 390, 74–86.

Caves, J.K., Jost, A.B., Lau, K.V., Maher, K., 2016. Cenozoic carbon cycle imbalances and a variable weathering feedback. Earth Planet. Sci. Lett. 450, 152–163.

Cerling, T.E., 1984. The stable isotopic composition of modern soil carbonate and its relationship to climate. Earth Planet. Sci. Lett. 71, 229–240.

Colbourn, G., Ridgwell, A., Lenton, T.M., 2013. The rock geochemical model (RokGeM) v0.9. Geosci. Model Dev. 6, 1543–1573.

Davidson, E.A., Samanta, S., Caramori, S.S., Savage, K., 2012. The dual Arrhenius and Michaelis–Menten kinetics model for decomposition of soil organic matter at hourly to seasonal timescales. Glob. Change Biol. 18, 371–384.

Dessert, C., Dupré, B., Gaillardet, J., François, L.M., Allègre, C.J., 2003. Basalt weathering laws and the impact of basalt weathering on the global carbon cycle. Chem. Geol. 202, 257–273.

Donnadieu, Y., Goddéris, Y., Pierrehumbert, R., Dromart, G., Fluteau, F., Jacob, R., 2006. A GEOCLIM simulation of climatic and biogeochemical consequences of Pangea breakup. Geochem. Geophys. Geosyst. 7, Q11019. https://doi.org/10.1029/2006GC001278.

Drever, J.I., 1997. The Geochemistry of Natural Waters: Surface and Groundwater Environments, third edition. Prentice-Hall, Upper Saddle River, NJ. 436 pp.

France-Lanord, C., Derry, L.A., 1997. Organic carbon burial forcing of the carbon cycle from Himalayan erosion. Nature 390, 65–67.

Gaillardet, J., Dupré, B., Louvat, P., Allègre, C.J., 1999. Global silicate weathering and $CO_2$ consumption rates deduced from the chemistry of large rivers. Chem. Geol. 159, 3–30.

Goddéris, Y., Joachimski, M.M., 2004. Global change in the late Devonian: modelling the Frasnian–Famennian short-term carbon isotope excursions. Palaeogeogr. Palaeoclimatol. Palaeloecol. 202, 309–329.

Goddéris, Y., Brantley, S.L., Francois, L., Schott, J., Pollard, D., Deque, M., Dury, M., 2013. Rates of consumption of atmospheric $CO_2$ through the weathering of loess during the next 100 yr of climate change. Biogeosciences 10, 135–148.

Godsey, S.E., Kirchner, J.W., Clow, D.W., 2009. Concentration–discharge relationships reflect chemostatic characteristics of US catchments. Hydrol. Process. 23, 1844–1864.

Helgeson, H.C., Murphy, W.M., Aagard, P., 1984. Thermodynamic and kinetic constraints on reaction rates among minerals and aqueous solutions. II. Rate constants, effective surface area, and the hydrolysis of feldspar. Geochim. Cosmochim. Acta 48, 2405–2432.

Ibarra, D.E., Caves, J.K., Moon, S., Thomas, D.L., Hartmann, J., Chamberlain, C.P., Maher, K., 2016. Differential weathering of basaltic and granitic catchments from concentration–discharge relationships. Geochim. Cosmochim. Acta 190, 265–293.

Keller, C.K., Wood, B.D., 1993. Possibility of chemical weathering before the advent of vascular land plants. Nature 364, 223–225.

Knapp, R.B., 1989. Spatial and temporal scales of local equilibrium in dynamic fluid–rock systems. Geochim. Cosmochim. Acta 53, 1955–1964.

Kump, L.R., Arthur, M.A., 1997. Global chemical erosion during the Cenozoic: weatherability balances the budgets. In: Ruddiman, W.R. (Ed.), Tectonic Uplift and Climate Change. Springer, Boston, MA, pp. 399–426.

Kump, L.R., Brantley, S.L., Arthur, M.A., 2000. Chemical weathering, atmospheric $CO_2$, and climate. Annu. Rev. Earth Planet. Sci. 28, 611–667.

Lagache, M., 1965. Contribution à l'étude de l'altération des feldspaths, dans l' eau, entre 100 et 200 °C, sous diverses pressions de $CO_2$, et application àla synthèse des minéraux argileux. Bull. Soc. Fr. Minéral. Cristallogr. 88, 223–253.

Li, L., Maher, K., Navarre-Sitchler, A., Druhan, J., Meile, C., Lawrence, C., Moore, J., Perdrial, J., Sullivan, P., Thompson, A., Jin, L., Bolton, E.W., Brantley, S.L., Dietrich, W.E., Mayer, K.U., Steefel, C.I., Valocchi, A., Zachara, J., Kocar, B., Mcintosh, J., Tutolo, B.M., Kumar, M., Sonnenthal, E., Bao, C., Beisman, J., 2017. Expanding the role of reactive transport models in critical zone processes. Earth-Sci. Rev. 165, 280–301.

Louvat, P., Allègre, C.J., 1997. Present denudation rates on the island of Réunion determined by river geochemistry: basalt weathering and mass budget between chemical and mechanical erosions. Geochim. Cosmochim. Acta 61, 3645–3669.

Lupker, M., France-Lanord, C., Galy, V., Lave, J., Gaillardet, J., Gajurel, A.P., Guilmette, C., Rahman, M., Singh, S.K., Sinha, R., 2012. Predominant floodplain over mountain weathering of Himalayan sediments (Ganga basin). Geochim. Cosmochim. Acta 84, 410–432.

Maher, K., 2011. The role of fluid residence time and topographic scales in determining chemical fluxes from landscapes. Earth Planet. Sci. 312, 48–58.

Maher, K., Chamberlain, C.P., 2014. Hydrologic regulation of chemical weathering and the geologic carbon cycle. Science 343, 1502–1504.

Maxwell, R.M., Condon, L.E., Kollet, S.J., Maher, K., Haggerty, R., Forrester, M.M., 2016. The imprint of climate and geology on the residence times of groundwater. Geophys. Res. Lett. 43, 701–708.

Moon, S., Chamberlain, C.P., Hilley, G.E., 2014. New estimates of silicate weathering rates and their uncertainties in global rivers. Geochim. Cosmochim. Acta 134, 257–274.

Moore, J., Lichtner, P.E., White, A.F., Brantley, S.L., 2012. Using a reactive transport model to elucidate differences between laboratory and field dissolution rates in regolith. Geochim. Cosmochim. Acta 93, 235–261.

Navarre-Sitchler, A., Thyne, G., 2007. Effects of carbon dioxide on mineral weathering rates at Earth surface conditions. Chem. Geol. 243, 53–63.

Palandri, J.L., Kharaka, Y.K., 2004. A Compilation of Rate Parameters of Water–Mineral Interaction Kinetics for Application to Geochemical Modeling. U.S. Geological Survey Open File Report 2004-1068. 64 pp.

Petsch, S.T., Berner, R.A., Eglinton, T.I., 2000. A field study of the chemical weathering of ancient sedimentary organic matter. Org. Geochem. 31, 475–487.

Raymo, M.E., Ruddiman, W.F., Froelich, P.N., 1988. Influence of late Cenozoic mountain building on ocean geochemical cycles. Geology 16, 649–653.

Stallard, R.F., Edmond, J.M., 1983. Geochemistry of the Amazon 2: the influence of geology and weathering environment on the dissolved load. J. Geophys. Res. 88, 9671–9688.

Steefel, C.I., Appelo, C.A.J., Arora, B., Jacques, D., Kalbacher, T., Kolditz, O., Lagneau, V., Lichtner, P.C., Mayer, K.U., Meeussen, J.C.L., Molins, S., Moulton, D., Shao, H., Simunek, J., Spycher, N., Yabusaki, S.B., Yeh, G.T., 2015. Reactive transport codes for subsurface environmental simulation. Comput. Geosci. 19 (3), 445–478.

Sundquist, E.T., 1991. Steady- and non-steady-state carbonate-silicate controls on atmospheric $CO_2$. Quat. Sci. Rev. 10, 283–296.

Thompson, J.B., 1959. Local equilibrium in metasomatic processes. In: Abelson, P.H. (Ed.), Researches in Geochemistry. John Wiley and Sons, New York, pp. 427–457.

Torres, M.A., West, A.J., Li, G., 2014. Sulphide oxidation and carbonate dissolution as a source of $CO_2$ over geological timescales. Nature 507, 346–349.

Uchikawa, J., Zeebe, R.E., 2008. Influence of terrestrial weathering on ocean acidification and the next glacial inception. Geophys. Res. Lett. 35, L23608. https://doi.org/10.1029/2008GL035963.

Urey, H.C., 1952. The Planets. Yale Univ. Press, New Haven, CT.

Velbel, M.A., 1993. Temperature-dependence of silicate weathering in nature – how strong a negative feedback on long-term accumulation of atmospheric $CO_2$ and global greenhouse warming. Geology 21 (12), 1059–1062.

Volk, T., 1987. Feedbacks between weathering and atmospheric $CO_2$ over the last 100 million years. Am. J. Sci. 287 (8), 763–779.

Walker, J.C.G., Hays, P.B., Kasting, J.F., 1981. A negative feedback mechanism for the long-term stabilization of Earth's surface temperature. J. Geophys. Res. 86, 9776–9782.

West, A.J., 2012. Thickness of the chemical weathering zone and implications for erosional and climatic drivers of weathering and for carbon-cycle feedbacks. Geology 40 (9), 811–814.

White, A.F., Brantley, S.L., 2003. The effect of time on the weathering of silicate minerals: why do weathering rates differ in the laboratory and field? Chem. Geol. 202, 479–506.

Winnick, M.J., Carroll, R.W.H., Williams, K.H., Maxwell, R.M., Dong, W., Maher, K., 2017. Snowmelt controls on concentration-discharge relationships and the balance of oxidative and acid-base weathering fluxes in an alpine catchment, East River, Colorado. Water Resour. Res. 53. https://doi.org/10.1002/2016WR019724.

Wolery, T.J., Jackson, K.J., Bourcier, W.L., Bruton, C.J., Viani, B.E., Knauss, K.G., Delany, J.M., 1990. Current status of the EQ3/6 software package for geochemical modeling. ACS Symp. Ser. 416, 104–116.

Zeebe, R., 2012. LOSCAR: long-term OCean–atmosphere sediment CArbon reservoir model v2.0.4. Geosci. Model Dev. 5, 149–166.